

Deep state-space modeling for explainable representation, analysis, and generation of professional human poses

Brenda Elizabeth Olivas-Padilla and Sotiris Manitsaris

Abstract—The analysis of human movements has been extensively studied due to its wide variety of practical applications, such as human-robot interaction, human learning applications, clinical diagnosis, and activity monitoring. Nevertheless, the state-of-the-art still faces scientific challenges while modeling human movements. Firstly, new models that account for the stochasticity of human movement and the physical structure of the human body are required to accurately predict the evolution of full-body motion descriptors over time. Secondly, the explainability of existing deep learning algorithms regarding their body posture predictions while generating human movements still needs to be improved as they lack comprehensible representations of human movement. This paper addresses these challenges by introducing three novel approaches for creating explainable representations of human movement. In this work, full-body movement is formulated as a state-space model of a dynamic system whose parameters are estimated using deep learning and statistical algorithms. The representations adhere to the structure of the Gesture Operational Model (GOM), which describes movement through its spatial and temporal assumptions. Two approaches correspond to deep state-space models that apply nonlinear network parameterization to provide interpretable posture predictions. The third method trains GOM representations using one-shot training with Kalman Filters. This training strategy enables users to model single movements and estimate their mathematical representation using procedures that require less computational power than deep learning algorithms. Ultimately, two applications of the generated representations are presented. The first is for the accurate generation of human movements, and the second is for body dexterity analysis of professional movements, where dynamic associations between body joints and meaningful motion descriptors are identified.

Index Terms—Article submission, IEEE, IEEEtran, journal, L^AT_EX, paper, template, typesetting.

I. INTRODUCTION

Movement is an essential component of human life. Humans are continually exchanging information and interacting with their surroundings through their movements, which result from complex and highly coordinated mechanical interaction between bones, muscles, ligaments, and joints within the musculoskeletal system. Through the study of this interaction and its effects, the structure, function, and motion of human bodies can be examined, and the resulting knowledge can be then used to improve the quality of human life.

The automatic analysis of human movements based on motion capture (MoCap) data as a research domain has increased

in significance due to the emergence of numerous applications in health, sports, motion-driven user interfaces, and intelligent surveillance.

Computer-based movement analysis serves the same purpose as a trainer, or another specialist who objectively examines motions. In order to do this, motion data must first be segmented. Then the tracked motion data is mapped into meaningful motion descriptions that the user can interpret. Depending on the motion-related application, various techniques such as statistical models or data-driven approaches, like machine learning or deep learning algorithms, can be used to model the human motion data. However, it remains complex and requires overcoming scientific challenges to design an accurate and versatile automatic analysis tool to describe human motion dynamics based on MoCap data. A first challenge would be achieving a high level of modeling accuracy. The system should consider human motion's stochasticity and body joints' mediations to accurately predict how human motion descriptors will evolve over time so that this information can be used proactively. Secondly, the models should be able to describe its outputs and assist humans in understanding how specific human motions are performed in order to properly employ this knowledge in an application.

This paper addresses the previous challenges through the analytical modeling of human motion dynamics. Accordingly, the following two hypotheses were formulated. The first hypothesis is that human motion dynamics can be modeled analytically by taking into account the interdependencies between joints as well as the dependencies between their prior values. Secondly, the cooperation of body joints and their contribution during the performance of a human movement can be learned and represented through interpretable models. To address these hypotheses, it was first investigated statistical and deep learning approaches for parameterizing the human motion mathematical representation. This investigation resulted in the creation of three novel approaches to represent and simulate human movement.

In this article, Section II reviews relevant research in human motion modeling. Section III introduces the three novel approaches for modeling human movements through interpretable mathematical representations. Next, Section VI presents and discusses the simulation performance of the three approaches with each dataset used. Section VII details the application of the trained motion representations for body dexterity analysis. Lastly, Section VIII provides conclusions of this work.

II. RELATED WORKS

A. Biomechanical modeling

Biomechanical models have generally been used to simulate human movement and the changes that occur as a result of internal and external action forces. These models represent the human body as a set of articulated links in a kinetic chain, with joint torques and forces calculated using anthropometric, postural, and hand load data [1]. Inverse dynamics is applied to extract quantitative information about the mechanics of the musculoskeletal system during the performance of a motor task. In previous studies [2]–[4], optical and inertial MoCap systems were utilized to measure the subject's posture as well as the position of an object. Then, along with the measurements of ground reaction forces with force plates, a kinematic analysis was done. The outcomes are afterward utilized by the inverse dynamic algorithm.

Developing precise and noninvasive methods in biomechanical modeling remains challenging. The need for new methods to analyze motions captured outside of laboratories arises as laboratory recordings lack authenticity. They are not done on the actual scenarios where the movements are performed, presumably leading to inaccurate measurements.

B. Stochastic modeling

Stochastic modeling has been used to learn the random behavior of human motion. These models utilize the variance information contained in body motion trajectories to predict and identify human intentions and actions. Among the most successful methods for dealing with the temporal variations of human movements are generative models, in which time series are reorganized by sequential states. A common approach to describing human motion in this way is by using state-space models (SSMs). Previous research applied SSMs based on Kalman filters for representing kinematic models to forecast pedestrian position trajectories [5], [6]. The Kalman filter (KF) was mostly used to track the position of pedestrians based on their estimated velocity or acceleration. Caramiaux et al. [7] introduced an adaptive SSM based on particle filtering that recognizes and continuously tracks the variations of gestures. Hidden Markov Models (HMMs) have proven successful in modeling the temporal evolution of gestures globally. Previous works [8]–[10] used HMMs to recognize gestures associated with professional tasks performed in the crafts and manufacturing industries. In another stochastic approach to model full-body movements, Wang et al. [11] proposed the Intention-Driven Dynamics Model that presupposes human dynamics change when actions are motivated by various intentions. Devanne et al. [12] used a Dynamic Naive Bayes model to capture the dynamics of motion primitives and continuously segment distinct human behaviors in extended sequences.

Despite these encouraging advances in recent years, accurate human motion modeling in unconstrained environments remains challenging. Unresolved difficulties in the modeling concern spatiotemporal dynamics. For example, even the same motion done by the same individual can have varying speeds and starting/ending positions, let alone in scenarios involving

multiple performers. Hybrid biomechanical-stochastic models have been developed to overcome these challenges.

C. Hybrid biomechanical-stochastic modeling

Biomechanical-stochastic models encapsulate the kinematic correlations among different skeletal joints besides capturing human motion stochastics. Biomechanical-stochastic modeling has been effectively used to research human movement variability and the prevention of a wide range of musculoskeletal system injuries [13], [14]. Lin et al. [15] proposed a hybrid model to predict the probability of injury and identify factors contributing to the risk of non-contact anterior cruciate ligament injuries. In another work, Donnell et al. [16] used a two-state Markov chain model to represent the survival of surgical repair from a torn rotator cuff. To simulate human motions and explain the interaction between joints for achieving the learned motion trajectories, the Gesture Operational Model (GOM) presented by Manitsaris et al. [10] has proven successful. Through state-space modeling, GOM's assumptions about joints' dynamic associations are converted into a simultaneous equation system. The equation system can then simulate human motion and describe the joints' interaction by examining the learned parameters.

A limitation of hybrid models is that their processing requirements grow exponentially as the number of model parameters increases. They are not practical for analyzing large datasets or high-dimensional MoCap data as data-driven approaches, requiring feature engineering. Moreover, to adequately design the models, it is necessary to have prior knowledge of the training data. Data-driven approaches do not require this prior knowledge since they generate their own internal representations based on the training data.

D. Data-driven approaches

The main advantage of data-driven approaches over other conventional statistical approaches is their great modeling capacity and considerable flexibility in designing architectures. The underlying similarity of motion forecasting and sequence-to-sequence prediction tasks has led research in this domain toward encoder-decoder architectures. Recent works have integrated skeletal representations to include spatial correlations among joints for the prediction of full-body human movements. Shu et al. [17] applied a co-attention mechanism for motion prediction that learned body joint spatial coherence and temporal evolution. Mao et al. [18] proposed three autoencoder (AE) with attention, which processed motion on distinct levels: the whole body, body parts, and single joints. Cai et al. [19] utilized the Discrete Cosine Transform to transform the motion into the frequency domain. The frequency components were then processed using a transformer-based architecture (global attention mechanism) in order to capture spatio-temporal correlations of the human pose.

Variational autoencoders (VAEs) have been applied for stochastic motion prediction, where they predict multiple and diverse motion sequences in the future from a single input sequence. Aliakbarian et al. [20] accomplished this through conditional VAE, whereas Mao et al. [21] used a VAE to

generate the motion of various body parts in a sequential manner. In order to enhance advances in probabilistic time series forecasting, Chung et al. [22] and Fraccaro et al. [23] used Recurrent Neural Networks (RNNs) to build connections between SSMs and VAEs. This led to deep SSMs, in which RNNs are used to parameterize the non-linear observation and transition models. For probabilistic forecasting, Salinas et al. [24] proposed the DeepAR, which uses auto-regressive RNNs with mean and standard deviation as output. Liu et al. [25] introduced a deep SSM based on Convolutional Neural Networks that provided a unified formulation for multiple human motion systems and enabled the accurate prediction of 3D human postures.

Even though there has been a lot of progress in modeling human motions recently, with neural networks (NNs) that make impressive predictions and simulations of human motions, as these approaches get more complicated, they become harder to understand and interpret their results. They can learn highly complex non-linear relationships from large datasets and surpass humans and other methods at many tasks. Nevertheless, their obscurity restricts their applicability and inspires little confidence among scientists and analysts who, for example, undertake the prognosis of movement disorders. So, while complex networks can handle activity recognition and event detection problems that put predictive accuracy above interpretability, models that can be intuitively interpreted, like analytical models, are better for applications that help people learn and improve their skills in handicrafts, industry, or sports, as well as for medical diagnostic and prognostic tools.

III. METHODOLOGY

This paper hypothesizes that human motion dynamics can be modeled by analytical models that can be interpreted and whose assumptions take into account the stochasticity of human motion and physical body structure. Consequently, given the nature of the hypotheses defined, GOM, a hybrid stochastic-biomechanical approach based on kinematic descriptors, was selected to model the dynamics of human movements and create interpretable representations for human motion trajectories. Representing human motion as a SSM of a dynamic system provides a simplified mathematical formalization of the motion phenomenon and approximates it to reality, for instance, through static or dynamic simulation. In addition, the mathematical representation of GOM permits a more intuitive description of how body joints cooperate (spatial dynamics) and evolve over time (temporal dynamics). GOM demonstrated to be effective at simulating human joint position trajectories. Furthermore, due to the usage of a transition function, it performs well with observations obtained from varied environments and subjects without requiring extensive training datasets [26]. This generalization capability is essential for applications requiring rapid and accurate analysis of varied human movements.

This paper presents three novel approaches for modeling human movements using full-body motion representations of GOM. The first method estimates the motion parameters using statistical modeling, whereas the second and third methods

employ RNNs. Each approach trains time-varying motion representations that can be utilized to simulate realistic human movements. The simulation performance achieved with each approach is evaluated and compared with that attained with the first GOM version proposed in [10], that uses constant motion representations. The schematic of the methodology followed in this paper is shown in Fig. 1.

IV. DATA COLLECTION

Diverse MoCap datasets have been made public for the analysis of human motion [27]–[31]. However, most of these available datasets consist of ordinary activities and sports motions recorded inside laboratories. For that reason, seven datasets presented and further detailed in X were used in this paper to analyze actual operators' and artisans' motions.

These datasets are composed of various professional movements captured in real-world scenarios. The recorded professional movements can be divided into three categories: industrial and crafts. Three datasets contain industrial tasks related to television assembly (TVA), packaging (TVP), and airplane assembly (APA), in total six operators were recorded. There is another dataset composed of motions of different ergonomic risk levels performed by ten subjects in a laboratory (ERGD). The last three correspond to motion data from four craftsmen engaged in glassblowing (GLB), silk weaving (SLW), and mastic cultivation (MSC).

For the creation of each dataset, the experts and subjects agreed to be recorded in their actual workplace while wearing the BioMed bundle motion capture system from Nansense Inc.¹. The system is composed of a full-body suit with 52 inertial sensors strategically positioned across the torso, limbs, and hands. At a rate of 90 frames per second, the sensors measure the orientation and acceleration of body segments on the articulated spine chain, shoulders, arms, legs, and fingertips. After a recording, the Euler local joint angles on the X, Y, and Z axes were automatically calculated through the Nansense Studio's inverse kinematics.

V. MOVEMENT REPRESENTATION

The three methods proposed in this paper parametrize the GOM representation of each motion of the seven datasets. The structure of this representation is described next.

GOM models full-body movements using an equation system of autoregressive models. Each model in this system learns the motion trajectory of one joint. Suppose, human motion is depicted as a sequence of human postures $P_t = [P_1, P_2, \dots, P_T] \in \mathbb{R}^{T \times N}$. T is the length of the posture sequence and $N = J \times D$, where J is the number of joints measured, and D is the number of dimensions that the joint's motion descriptor is decomposed. The number of models in the equation system is equal to the number of dimensions associated with a given body joint (D), multiplied by the number of body joints (J) defined in GOM.

Inside these N models are four different assumptions regarding the dynamic relationship between body joints and their temporal dependencies:

¹Baranger Studios, Los Angeles, CA, USA

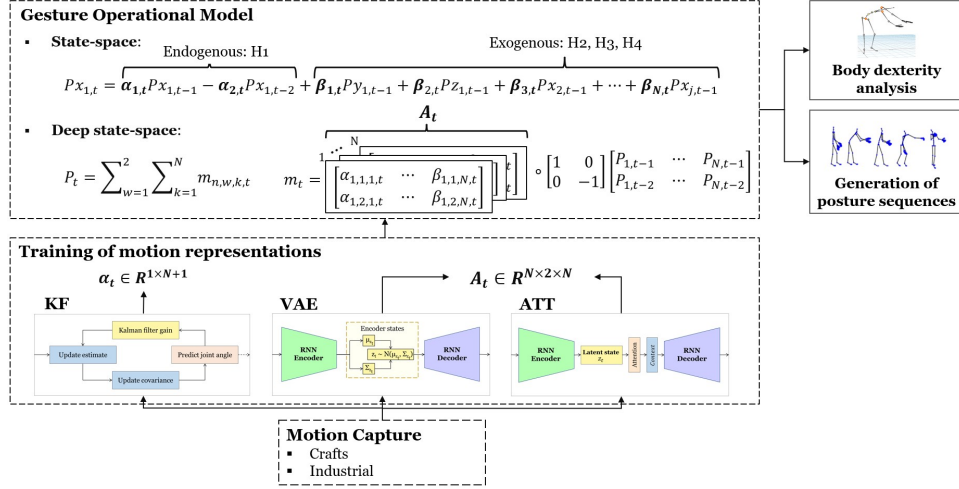


Fig. 1. Methodology for the creation and validation of the motion-based methods to simulate and describe human movement.

- H1** Transitioning: Velocity of the movement.
- H2** Intra-joint association: Movement of the body joint across the 3D space.
- H3** Inter-limb synergies: Cooperation and synchronisation between body limbs.
- H4** Serial and non-serial intra-limb mediations: Cooperation between serially and nonserially linked joints of the body.

Each assumption consists of a specific set of variables (in this case local joint angles) that are parametrized and depict a particular relationship between body joints or a temporal dependency. By examining the generated coefficients and statistical significance of each variable, it can be gleaned how relevant these are according to the movement modeled and the predicted joint angles. Human postures are expressed as 3D Euler joint angles in order to generate motions with subjects of various morphologies. Unlike joint positions, Euler joint angles are unaffected by identity-specific body shape. Moreover, Euler angles can be intuitively interpreted in the analytical model and provide a more clear illustration of how human movements are conducted.

A diagram of GOM and its assumptions is provided in Fig. 2, along with the joints measured for the modeling of the full-body movements. For the purposes of this work, only measurements from 19 inertial sensors were used for the modeling. Discarding MoCap data from the fingers and feet to simplify the human motion representation. Thus, 57 joint angles were modeled in GOM. An example of the estimated mathematical representations of n assumptions for one joint angle with time-varying coefficients $\alpha_{n,t}$ is illustrated in (1).

$$Px_{1,t} = \underbrace{\alpha_{1,t}Px_{1,t-1} - \alpha_{2,t}Px_{1,t-2}}_{H1} + \underbrace{\alpha_{3,t}Py_{1,t-1} + \alpha_{4,t}Pz_{1,t-1}}_{H2} + \underbrace{\alpha_{5,t}Px_{2,t-1} + \dots + \alpha_{n,t}Px_{j,t-1}}_{H3 \text{ or } H4} \quad (1)$$

The model represents the angle trajectory of the body joint $P_{1,t}$ at time t on the X-axis ($Px_{1,t}$). The $P_{1,t}$ joint's motion is decomposed on XYZ axes ($Px_{1,t}$, $Py_{1,t}$, and $Pz_{1,t}$) and has an association with j body parts. Furthermore, GOM's

models are second-order autoregressive models due to the correlation between lag values (auto-correlation) in the time series. Overall, the GOM structure used in this work comprises 57 models as (1), each of which represents a joint motion trajectory.

The trained GOM can be utilized for two main applications. First, the joint angle trajectories of each modeled motion can be simulated by solving the simultaneous equation system that composes GOM. The second is that, as an analytical model, the trained models can be used to obtain insights into the dynamic relationship between body joints during the performance of a movement. This dexterity analysis corresponds to describing the movement of each joint based on the learned parameters from its mathematical representation. Following, it is described the three different approaches to trained the GOM representation. These are later evaluated in Section VII.

A. Learning of constant and time-varying GOM representations using one-shot learning

The first approach trains GOM representations using one-shot training with KF. The fundamental concept is to formulate each joint angle model as a separate SSM and then use KF to compute the log-likelihood of the observed joint angle data for a given set of parameters.

Suppose that the joint angle on the X-axis of a body part, $Px_{1,t}$, is modeled. Its GOM representation consists of the (1). The observation would be the real joint angle, $y_t = Px_{1,t}$, where $Px_{1,t} \in \mathbb{R}^{1 \times 1}$, and the variables from the assumptions H2, H3, and H4 correspond to the exogenous input x_t . The following log-likelihood is then maximized with respect to θ and α , utilizing the KF to calculate the log-likelihood for each time t :

$$\ell(\theta, \alpha) = \sum_{t=1}^T \log p_{\theta}(y_1, \dots, y_{t-1} | x_1, \dots, x_{t-1}) \quad (2)$$

θ corresponds to the tuning parameters of the KF, whereas α constitutes the coefficients of the overall GOM representation, $\alpha = [A, B]$. A corresponds to the coefficients of assumption

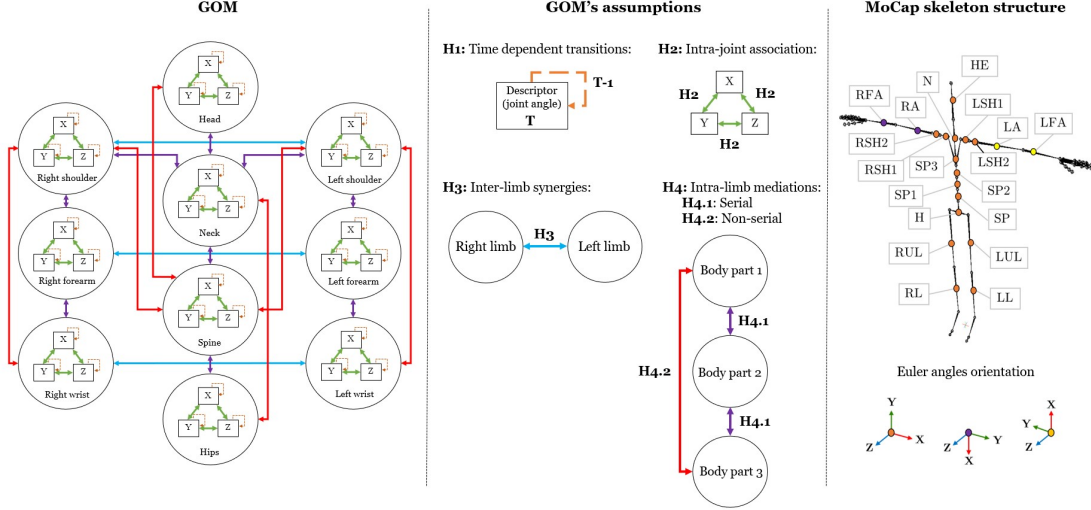


Fig. 2. The Gesture Operational Model and its assumptions. The mathematical representation of GOM is utilized to model the movements of every joint of the MoCap skeleton. Then, the full-body movement is simulated and explained using each joint's motion model.

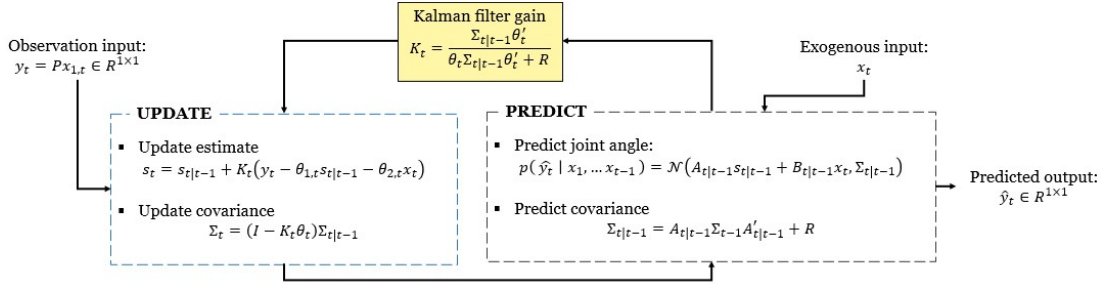


Fig. 3. Flow chart of the iterative process of the KF while doing MLE for estimating GOM's coefficients.

H1, and B the coefficients for the rest of the assumptions. The diagram of the iterative process of the Kalman filter for calculating the likelihood in (2) for every time t is illustrated in Figure 3. Note that \hat{y}_t corresponds to the joint angle prediction using the motion representation in (1) with the estimated coefficients α . The preceding approach is repeated for every joint angle model in GOM. This results in 57 motion representations that can be used to simulate full-body movements.

B. Data-driven strategies for estimating time-varying GOM representations

By taking advantage of the modeling power of NNs, both approaches train all motion representations of GOM simultaneously. To this end, now the observations are defined as $y_t = P_t \in \mathbb{R}^{1 \times N}$, meaning the N joint angles at time t that compose the whole body posture P_t , and $x_t = [P_{t-1}, P_{t-2}] \in \mathbb{R}^{2 \times N}$.

The decoders from both frameworks have the full-body GOM mathematical representations as the output layer. The decoder calculates the coefficients $\alpha_t = [\alpha_1 \cdots \alpha_N]$, which are then utilized by the GOM equation system to produce the prediction \hat{y}_t . Since GOM employs a second-order equation system, each element in α_t corresponds to a 2D tensor with the shape $(2, N)$. N because all joint angles are included in

each GOM equation as the assumptions (H2, H3, and H4), and two vectors as it also computed the coefficients of the transition assumptions (H1). Thus, being x_t and α_t tensors of shape $(2, N)$ and $(N, 2, N)$, respectively, the procedure for generating \hat{y}_t utilizing the GOM representations in the decoder is as follows:

$$m_t = \alpha_t \circ \begin{bmatrix} 1 & 0 \\ 0 & -1 \end{bmatrix} x_t \quad (3)$$

$$\hat{y}_t = \sum_{w=1}^2 \sum_{k=1}^N m_{t,i,w,k} \quad (4)$$

where \circ is an element-wise product, $\hat{y}_t \in \mathbb{R}^{1 \times N}$, and $m_t \in \mathbb{R}^{N \times 2 \times N}$. m_t corresponds to GOM in a matrix form, consisting of the 57 joint angle models as Equation 1.

VAE-RGOM and ATT-RGOM are composed of RNNs for the encoder and decoder, representing human motions similarly to KF-GOM and KF-RGOM as a state-space model. These were trained to maximize the following likelihood, approximating $\hat{y}_{1:T}$ as close as possible to the system's observed $y_{1:T}$:

$$p_\theta(\hat{y}_{1:T} | x_{1:T}) = \int \underbrace{p_\theta(\hat{y}_{1:T} | z_{1:T}, x_{1:T})}_{\text{Observation model}} \underbrace{p_\theta(z_{1:T} | x_{1:T})}_{\text{Transition model}} dz_{1:T} \quad (5)$$

where $z_{1:T}$ represents the states of the system, and $x_{1:T}$ is the input that, with $z_{1:T}$, generates the outputs $\hat{y}_{1:T}$. The generative model in Equation 5 is composed of an observation model represented as $p_\theta(\hat{y}_{1:T}|z_{1:T}, x_{1:T})$ and a transition model represented as $p_\theta(z_{1:T}|x_{1:T})$:

$$p_\theta(\hat{y}_{1:T}|z_{1:T}, x_{1:T}) = \prod_{t=1}^T p_\theta(\hat{y}_t|z_t, x_t) \quad (6)$$

$$p_\theta(z_{1:T}|x_{1:T}) = \prod_{t=1}^T p_\theta(z_t|z_{t-1}, x_t) \quad (7)$$

The parameters θ from the observation and transition models are learned during training by the decoder of each framework.

In each approach, the encoder has a different function, taking advantage of their very specific encoder-decoder architecture. In VAE-RGOM, the encoder functions as an inference network, whereas in ATT-RGOM, it initializes the system's state as a selected sequence of observed joint angles. However, for both approaches, the decoder's goal is to learn the state transition in order to update the system's state and produce the desired future posture \hat{y}_t .

VAE-RGOM and ATT-RGOM seek to maximize the marginal log-likelihood below:

$$\text{Maximum } \ell(\theta, \varphi) = \sum_{t=1}^T \log p_\theta(\hat{y}_{1:T}|x_{1:T}) \quad (8)$$

In VAE-RGOM similar to a conventional VAE, the encoder estimates the stochastic latent states z by approximating $q_\varphi(z_t|x_t, y_t)$ to the true posterior distribution $p_\theta(z_t|z_{t-1}, x_t)$ defined by a mean μ_{z_t} and a log covariance Σ_{z_t} . Stochastic gradient optimization was used to train the networks. This entails first sampling z_t , subsequently estimating the ELBO, then the gradients for θ , φ , and α , and lastly, updating these parameters. The loss of Equation 8 is thus equivalent to the maximum ELBO with respect to θ , φ , and α that results:

$$\ell(\theta, \varphi, \alpha) = \sum_{t=1}^T \underbrace{-\beta_{\text{VAE}} \text{KL}(q_\varphi(z_t|z_{t-1}, x_t, y_t) || p_\theta(z_t|z_{t-1}, x_t))}_{\text{Regularization loss}} + \underbrace{\beta_{\text{GOM}} \mathbb{E}_{q_\varphi(z_t|z_{t-1}, x_t, y_t)} [\log p_\theta(y_t|z_t, x_t)]}_{\text{Prediction loss}} \quad (9)$$

In Equation 9, KL denotes the Kullback-Leibler divergence that captures the complexity of the data; the prediction loss measures the accuracy of the model in the prediction; β_{VAE} and β_{GOM} correspond to tuning hyperparameters. Instead of directly sampling from q_φ at each time step, $z_t = \mu_{z_t} + \epsilon \odot \Sigma_{z_t}$ is re-parametrized using samples from a normal random variable $\epsilon \sim \mathcal{N}(0, I)$. Consequently, the gradients relative to the parameters θ , φ , and α can be back-propagated through the encoder via the sampled z_t . As the prediction loss, the mean absolute difference of all joint angles is employed:

$$\ell_{\text{euler}} = \frac{1}{J} \sum_{j=1}^J \frac{1}{D} \sum_{d=1}^D \|P_{t,j,d} - \hat{P}_{t,j,d}\|_1 \quad (10)$$

ATT-RGOM parameterizes a state-space system by using its LSTM encoder to initialize the system's state z_t as a context vector c_t of the observed joint angles. The context vector is

determined by the sequence of hidden states $h_{1:T}$ to which the encoder maps the input sequence $x_{1:T}$ of length T . The LSTM decoder models the state transition $p_\theta(z_t|z_{t-1}, c_t)$ in order to update the system's state and generate the future posture $p_\theta(y_t|z_t, x_t)$.

The Luong attention mechanism is integrated in order to capture state dynamics. The attention mechanism takes previous postures into account and maps them to attention weights (w_t), computed using a dot product alignment. The attention weights determine the degree to which previous hidden states $h_{1:T}$ influence future state transitions. This influence is indicated in the context vector, which is the weighted sum of the h_i :

$$c_t = \sum_{i=1}^T w_{t,i} h_i \quad (11)$$

In accordance with the model structure of AE with Luong attention mechanism, the context vector is first used to compute the attentional hidden state \hat{s}_t . The decoder then uses this state to generate the GOM's coefficients, followed by \hat{y}_t .

In order to tune the VAE-RGOM's and ATT-RGOM's hyperparameters, a Bayesian optimization was carried out based on the loss achieved on a validation set [32]. The best architecture of each network is described in tables I and II.

VI. STATIC AND DYNAMIC SIMULATION OF PROFESSIONAL MOVEMENTS

This section evaluates KF-RGOM, VAE-RGOM, and ATT-RGOM in terms of their ability to simulate realistic human movements. Their performances are compared with the first approach denoted as KF-RGOM proposed in [10]. In KF-RGOM, constant GOM representations are learned using one-shot training with KF. Each approach predicted one time step per iteration. After predicting all the time frames of a movement, the simulated movement was compared with the original for evaluation. A reference motion was utilized for the training of the KF-RGOM and KF-GOM. Regarding the training of VAE-RGOM and ATT-RGOM, these were trained with all seven datasets using an NVIDIA GPU RTX 2060, and applying 80-10-10 sets (80% for training, 10% for validation, and 10% for testing). The validation set was used to estimate the neural networks' hyperparameters, while the test set was utilized for evaluation.

To complement the analysis of the full-body simulations generated with the deep SSMs, visual comparisons between the quality of the generated sequences and the ground truth sequence are offered in figures 6 and 7. The red boxes show variations in the generated motions at different temporal windows.

The experiments suggest that by solving the simultaneous equations that compose the GOM, it is possible to accurately simulate diverse human motions using Euler joint angles as motion descriptors. Overall, time-varying GOM representations are tolerant of slight variations in human motions and offsets between motions of the same class produced by varying recording conditions (different subjects or different recording days). Implementing time-varying coefficients increased the modeling performance of GOM, especially for motions with

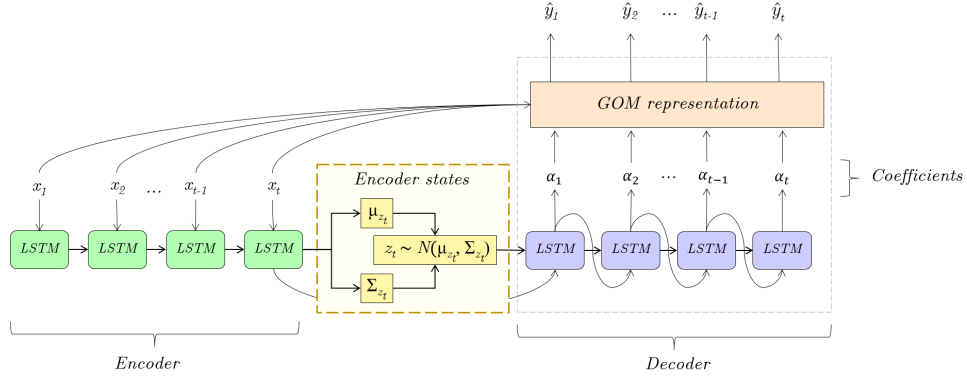


Fig. 4. Overview of the Variational Autoencoder network for estimating GOM's coefficients.

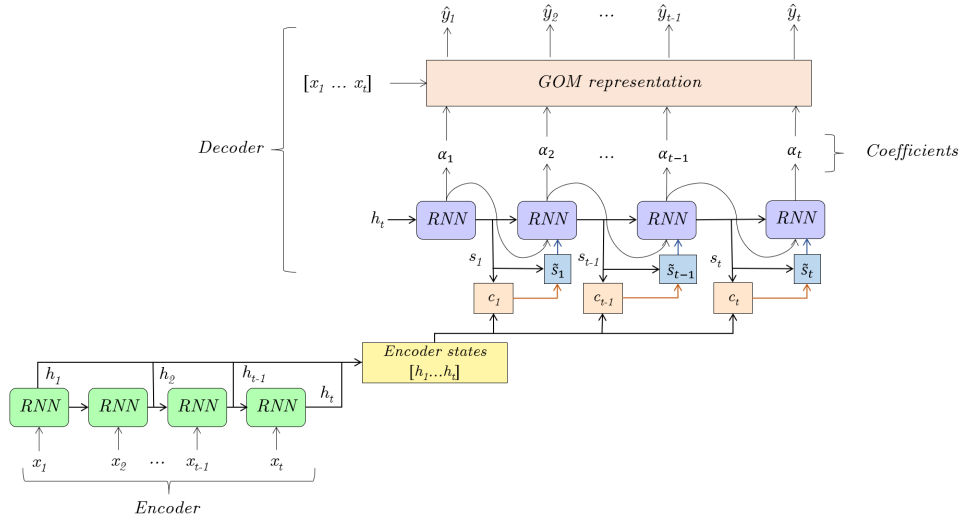


Fig. 5. Overview of the Autoencoder with Luong Attention for estimating GOM's coefficients.

TABLE I
VAE-RGOM ARCHITECTURE.

Layer	Type	Output shape	Activation	Dropout	Rdrop	Input layer
1	Input	(2,57)	-	-	-	-
2	LSTM	(2,32)	Softsign	0.2	0.2	1
3 (μ_{z_t})	FC	2	Linear	-	-	2
4 (Σ_{z_t})	FC	2	Linear	-	-	2
5 (z_t)	Sampling	2	-	-	-	3,4
6	LSTM	(2,32)	Softsign	0.2	0.2	5
7	Dropout	(2,32)	-	0.8	-	6
8	TFC	(2,3249)	Linear	-	-	7
9 (α_t)	Reshape	(57,2,57)	-	-	-	8
10 (GOM)	Lambda	(1,57)	-	-	-	1,9

TABLE II
ATT-RGOM ARCHITECTURE.

Layer	Type	Output shape	Activation	Dropout	Rdrop	Input layer
1	Input	(2,57)	-	-	-	-
2	LSTM	2.1 Output state:(2,32) 2.2 Hidden state: 32 2.3 Cell state: 32	Softsign	0.2	0.2	1
3	BatchN	32	-	-	-	2.2
4	BatchN	32	-	-	-	2.3
5	LSTM	(2,32)	Softsign	0.2	0.2	3, 4
6	Dot	(2,2)	-	-	-	2.1, 5
7 (w_t)	Softmax	(2,2)	-	-	-	6
8 (c_t)	Dot	(2,32)	-	-	-	2.1, 7
9	Concatenate	(2,64)	-	-	-	5, 8
10	TFC	(2,3249)	Linear	-	-	9
11 (α_t)	Reshape	(57,2,57)	-	-	-	10
12 (GOM)	Lambda	(1,57)	-	-	-	1, 11

TABLE III
MEAN ABSOLUTE ANGLE ERRORS FOR EACH DATASET.

Dataset	KF-GOM	KF-RGOM	VAE-RGOM	ATT-RGOM
TVA	16.830 (σ : 15.379)	6.938 (σ : 0.459)	0.093 (σ : 0.016)	0.191 (σ : 0.024)
TVP	7.947 (σ : 5.278)	9.867 (σ : 5.592)	0.213 (σ : 0.058)	0.398 (σ : 0.085)
APA	3.312 (σ : 2.816)	10.946 (σ : 0.664)	0.091 (σ : 0.019)	0.203 (σ : 0.048)
GLB	19.211 (σ : 9.981)	12.916 (σ : 3.665)	0.119 (σ : 0.044)	0.220 (σ : 0.066)
SLW	14.267 (σ : 7.739)	9.207 (σ : 3.307)	0.115 (σ : 0.041)	0.246 (σ : 0.078)
MSC	23.313 (σ : 14.514)	16.002 (σ : 5.887)	0.247 (σ : 0.101)	0.457 (σ : 0.126)
ERGD	13.461 (σ : 8.699)	13.569 (σ : 4.931)	0.095 (σ : 0.052)	0.198 (σ : 0.085)

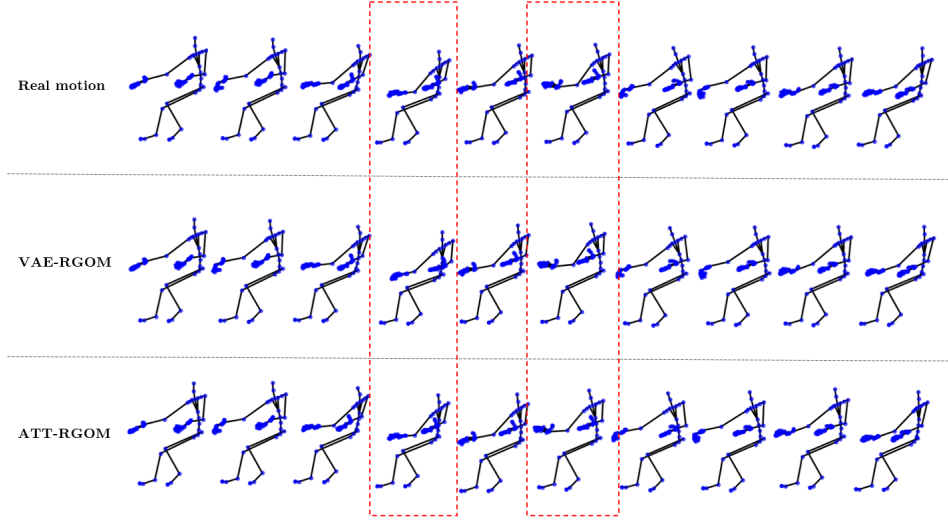


Fig. 6. Visual comparison of generated posture sequences from GLB and its ground-truth. The glassblower rotates the blowpipe with the left hand while shaping the glass with the right.

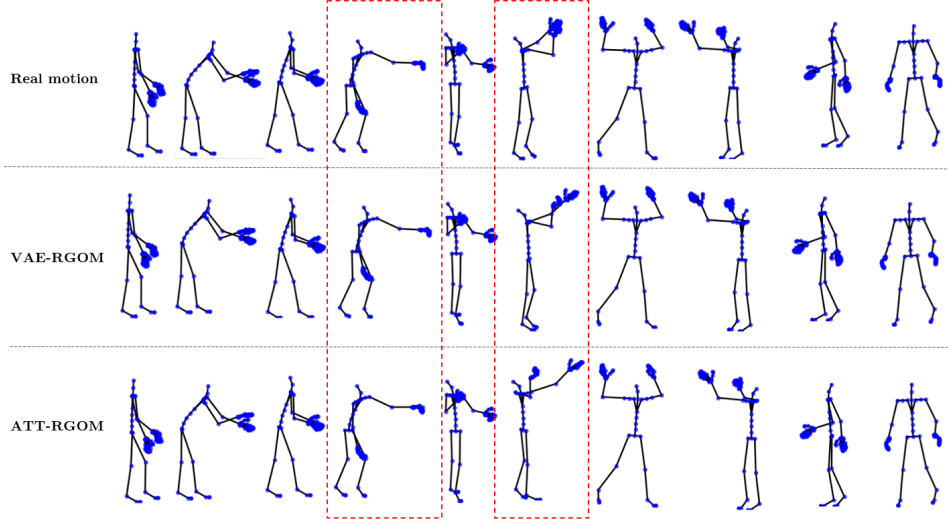


Fig. 7. Visual comparison of generated posture sequences from TVP and its ground-truth. The operator places a television on the third level of a pallet.

greater variance and longer duration, such as those conducted during glassblowing. This is due to the fact that coefficients were adapted to the change in mediations between the dependent variables and their assumptions throughout the whole time series.

Across all seven datasets, the time-varying parameter models estimated by data-driven approaches performed the best. Two arguments were deduced as to why this improvement in performance. First, both deep SSMs used motion data from all seven datasets for training, which would have allowed them to map diverse relationships between assumptions and dependent variables and accurately estimate the optimal coefficients for one-step prediction. The variability between the training motion and test motions may account for the errors exhibited by both KF-GOM and KF-RGOM. Accordingly, it can be inferred that the quality of their simulations depends on the recorded person's ability to replicate their movements while repeatedly

performing the same activity.

Secondly, the temporal encoder-decoder structure of VAE-RGOM and ATT-RGOM enables these models to learn a low-dimensional (latent space) manifold of the data. Ideally, this manifold untangles variation factors across distinct movements, clusters related motion descriptors, and aids in identifying joint dynamics across sequences. In the case of VAE-RGOM, it disentangles the dynamics and postures in terms of the ELBO. For ATT-RGOM, this latent space allows the attention mechanism to interpret the hidden mechanisms and connections underlying the motion descriptors sequences.

According to the presented metrics, VAE-RGOM gave the most accurate movement simulations. VAE-RGOM may outperform ATT-RGOM since it models a probability distribution over future postures rather than making point estimates. Particularly, VAE-RGOM yields the highest simulation performance for motions from the datasets ERGD and TVA. These datasets

are the largest ones and correspond to the simplest movements with low intraclass variability. In these, the movements were performed in a more controlled setting. For instance, in ERDG, the subjects performed diverse motions in a laboratory, receiving constant instructions on how to perform them. In the case of TVA, the operators were recorded in a production cell performing the same tasks repeatedly for several hours with little variation in between repeats. In addition, the movements in TVA primarily involved manipulating objects with their hands. In contrast to the movements performed, for instance, by the craftsmen and farmers, who had to employ their entire bodies to perform their work properly.

The most challenging movements to replicate were those associated with mastic cultivation. The reason behind this could be a bias in the training data, as MSC was the smallest dataset and involved motions where the farmer most of the time moved while kneeling. In the other six datasets, the subjects were mostly standing while performing their tasks. This may have prevented the networks from fully learning the dynamics of the legs when they are flexed. Because when the farmer moved to reach the tree or objects, he usually repositioned the legs while kneeling to improve balance.

VII. BODY DEXTERITY ANALYSIS OF EXPERT PROFESSIONALS

A. Statistical analysis of human motion representations

The following are two examples of models with time-varying coefficients. These are summarized in tables, displaying the various representations provided by KF-RGOM, VAE-RGOM, and ATT-RGOM for the same movement. The equation is presented first with their corresponding assumptions and time-varying coefficients $\alpha_{i,t}$, where i is the number of coefficients. Next, the summary of their coefficients and p-values calculated for each time step is presented. The mean and standard deviation of the coefficients are provided, together with the range of p-values. The range indicates the highest and lowest p-values that were calculated over all time steps. Lastly, the posture sequence of the motion modeled in each equation is also given in a figure, along with the color annotations.

The first time-varying model is for the motion TVA₁, which consists of an operator grabbing a circuit board from a container. The joint angle on the Y-axis of the right arm (RAy) is modeled and represented in Equation 12. Tables IV, V, and VI present the summaries of coefficients and p-values estimated by each approach. Figure 8 illustrates the posture sequence and highlights the assumptions shown in Equation 12.

$$\begin{aligned} RAY_t = & \alpha_{1,t}RAY_{t-1} + \alpha_{2,t}RAY_{t-2} \\ & + \alpha_{3,t}RAX_{t-1} + \alpha_{4,t}RAZ_{t-1} \\ & + \alpha_{5,t}LAY_{t-1} + \alpha_{6,t}RSH1y_{t-1} \\ & + \dots + \alpha_{7,t}RFAy_{t-1} \end{aligned} \quad (12)$$

According to each table, the time-varying coefficients show a time dependence, being a low-speed motion; however, at certain periods of the time series, the values two time steps prior to the prediction were not significant in the KF-RGOM representation. All estimated representations exhibit an intra-joint association with the X and Z axes of RA (RAX and

RAZ). There is also an inter-limb synergy, but according to the coefficients provided by VAE-RGOM and ATT-RGOM, it was not significant for some periods of the time series. This indicates that there was not always a relationship between the movements of the right arm and the left arm, which could be the case if the operator was simply holding the card with the right hand. Lastly, there is a serial intra-limb mediation with RSH1 and RFA for KF-RGOM's and VAE-RGOM's representation. For ATT-RGOM, though, the mediation with RSH1 and RFA was not present throughout the entire time series. Specifically, RSH1 and RFA were not significant on transitions where the operator is walking toward the container or just standing and holding the circuit board for a moment.

The second example is a time-varying model of GLB₄, which corresponds to the motion of shaping the glass decanter curves with a wooden block while turning the blowpipe with the right hand. The Equation 13 represents the left shoulder's motion along the X-axis ($LSH2x_t$). Tables VII, VIII, and IX summarize each approach's estimated coefficients and their respective p-values. The posture sequence is illustrated in Figure 9.

$$\begin{aligned} LSH2x_t = & \alpha_{8,t}LSH2x_{t-1} + \alpha_{9,t}LSH2x_{t-2} \\ & + \alpha_{10,t}LSH2y_{t-1} + \alpha_{11,t}LSH2z_{t-1} \\ & + \alpha_{12,t}RSH2x_{t-1} + \alpha_{13,t}LAX_{t-1} \\ & + \dots + \alpha_{14,t}LFAx_{t-1} + \alpha_{15,t}SP3x_{t-1} \end{aligned} \quad (13)$$

The statistical analysis of each representation reveals a temporal dependency, indicating that the motion is slow. According to KF-RGOM and VAE-RGOM, there is an intra-joint association for all time series with $LSH2y$ and $LSH2z$, except for ATT-RGOM with respect to $LSH2y$. The motion presents an inter-limb synergy with $RSH2y$, indicated by KF-RGOM, VAE-RGOM, and ATT-RGOM, as it was as well for KF-GOM. This suggests a collaboration between both arms.

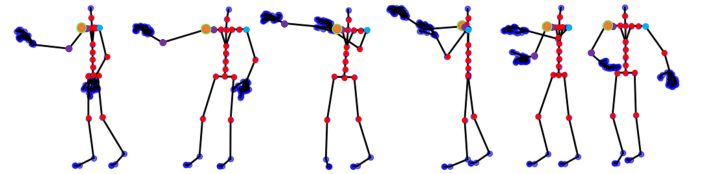


Fig. 8. Illustration of the movement performed in TVA₁, where the operator grabs from a container a circuit board. The color annotations are based on the assumptions of Equation (12).

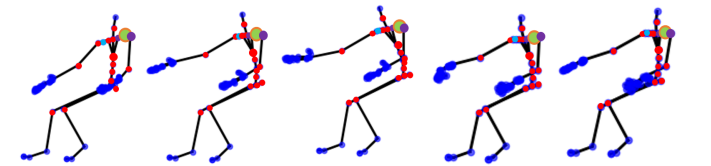


Fig. 9. Illustration of the movement performed in GLB₄, where the expert glassblower shapes the decanter curve with a block and simultaneously rotates the blowpipe back and forward. The color annotations are based on the assumptions of Equation (13).

TABLE IV
KF-RGOM: TVA₁.

Variable	Coefficients $\mu_\alpha(\sigma_\alpha)$	P-values [min, max]
$\alpha_{1,t}$	0.486 (0.014)	[0.001, 0.004]
$\alpha_{2,t}$	-0.096 (0.009)	[0.078, 0.220]
$\alpha_{3,t}$	-1.236 (0.007)	[0.001, 0.010]
$\alpha_{4,t}$	-0.273 (0.002)	[0.001, 0.005]
$\alpha_{5,t}$	-0.005 (0.03)	[0.001, 0.040]
$\alpha_{6,t}$	-4.711 (0.010)	[0.001, 0.015]
$\alpha_{7,t}$	0.156 (0.020)	[0.026, 0.040]

TABLE V
VAE-RGOM: TVA₁.

Variable	Coefficients $\mu_\alpha(\sigma_\alpha)$	P-values [min, max]
$\alpha_{1,t}$	1.089 (0.012)	[0.001, 0.005]
$\alpha_{2,t}$	0.051 (0.006)	[0.001, 0.010]
$\alpha_{3,t}$	-0.068 (0.003)	[0.001, 0.014]
$\alpha_{4,t}$	0.108 (0.002)	[0.001, 0.004]
$\alpha_{5,t}$	-0.001 (0.001)	[0.001, 0.474]
$\alpha_{6,t}$	-0.024 (0.002)	[0.001, 0.004]
$\alpha_{7,t}$	-0.003 (0.003)	[0.001, 0.020]

TABLE VI
ATT-RGOM: TVA₁.

Variable	Coefficients $\mu_\alpha(\sigma_\alpha)$	P-values [min, max]
$\alpha_{1,t}$	0.688 (0.012)	[0.001, 0.004]
$\alpha_{2,t}$	0.309 (0.030)	[0.001, 0.008]
$\alpha_{3,t}$	-0.506 (0.012)	[0.001, 0.011]
$\alpha_{4,t}$	-0.100 (0.006)	[0.001, 0.004]
$\alpha_{5,t}$	-0.007 (0.015)	[0.157, 0.499]
$\alpha_{6,t}$	0.009 (0.012)	[0.003, 0.496]
$\alpha_{7,t}$	-0.001 (0.003)	[0.028, 0.499]

TABLE VII
KF-RGOM: GLB₅.

Variable	Coefficients $\mu_\alpha(\sigma_\alpha)$	P-values [min, max]
$\alpha_{8,t}$	0.543 (0.001)	[0.001, 0.005]
$\alpha_{9,t}$	0.456 (0.009)	[0.001, 0.002]
$\alpha_{10,t}$	0.223 (0.017)	[0.001, 0.020]
$\alpha_{11,t}$	0.192 (0.026)	[0.001, 0.010]
$\alpha_{12,t}$	-0.087 (0.037)	[0.018, 0.045]
$\alpha_{13,t}$	0.011 (0.002)	[0.001, 0.003]
$\alpha_{14,t}$	-0.002 (0.001)	[0.053, 0.060]
$\alpha_{15,t}$	0.135 (0.001)	[0.045, 0.087]

TABLE VIII
VAE-RGOM: GLB₅.

Variable	Coefficients $\mu_\alpha(\sigma_\alpha)$	P-values [min, max]
$\alpha_{8,t}$	0.483 (0.003)	[0.001, 0.007]
$\alpha_{9,t}$	0.343 (0.001)	[0.001, 0.014]
$\alpha_{10,t}$	0.060 (0.001)	[0.001, 0.033]
$\alpha_{11,t}$	-0.094 (0.001)	[0.001, 0.002]
$\alpha_{12,t}$	0.016 (0.004)	[0.001, 0.009]
$\alpha_{13,t}$	0.066 (0.009)	[0.001, 0.005]
$\alpha_{14,t}$	-0.042 (0.004)	[0.001, 0.011]
$\alpha_{15,t}$	0.006 (0.001)	[0.007, 0.015]

TABLE IX
ATT-RGOM: GLB₅.

Variable	Coefficients $\mu_\alpha(\sigma_\alpha)$	P-values [min, max]
$\alpha_{8,t}$	0.444 (0.008)	[0.001, 0.006]
$\alpha_{9,t}$	0.348 (0.011)	[0.002, 0.018]
$\alpha_{10,t}$	0.022 (0.034)	[0.134, 0.161]
$\alpha_{11,t}$	-0.083 (0.010)	[0.001, 0.005]
$\alpha_{12,t}$	0.014 (0.003)	[0.002, 0.023]
$\alpha_{13,t}$	0.048 (0.003)	[0.001, 0.002]
$\alpha_{14,t}$	-0.013 (0.005)	[0.021, 0.144]
$\alpha_{15,t}$	-0.024 (0.017)	[0.029, 0.043]

As visualized in Figure 9, the glassblower manipulated the molten glass with one arm while rotating it with the other. This action requires synchronization between both arms, which is reflected in the representations of all four approaches. Again, all methods considered a non-serial intra-limb mediation with LFA. There is also a mediation with SP3 in all the representations. Similarly to the representation from KF-GOM, the p-value of SP3 was near the threshold in the representation of KF-RGOM and ATT-RGOM. Accordingly, the movement of the upper part of the spine is crucial when performing this particular movement in glassblowing. This may also be observed in Figure 9, where the glassblower moves his arms while bending his torso back and forth.

The preceding examples showed how the trained analytical models can be utilized to explain the physical dexterity of operators, craftsmen, and laboratory subjects. The models emphasized the key motion descriptors associated with and contributing to complex whole-body motion. This information can later be utilized to test skill acquisition strategies. A novice can learn to make precise motions by minimizing the variability of their motion representations compared to those of professional artisans or operators.

B. Selection of the most significant sensors to maximize recognition accuracy

This section explains how the best motion descriptors for modeling and recognizing a set of human movements from each dataset are determined according to the trained GOM representations. After performing the statistical analysis, the number of times a motion descriptor (assumption) is statistically significant for all equations that comprise GOM is counted. Then for the selection, different combinations of descriptors considered most frequently significant were utilized for training in an all-shots approach. Because a single inertial sensor gives three joint angles, all of the sensor's joint

angles were used for recognition if at least one was among the joint angles that were more often significant in all motions of a dataset.

For the recognition of human movements utilizing different sensor combinations, HMMs were trained. In order to properly train the HMMs, a gesture vocabulary containing the motions with the most iterations was specified for each dataset. The total number of motion classes for TVA, APA, and ERGD were four, three, and 28, respectively. The TVP, GLB, and MSC gesture vocabularies contained only motions with at least seven repetitions. Therefore, their respective gesture vocabularies included five, seven, and six classes of motion. Regarding SLW, the gesture vocabulary consisted of only three classes of silk weaving on a loom.

All gesture vocabularies were subjected to the selection process described previously with each approach's representations. Then, the sensor configurations that achieved the best performance were compared to the recognition performance obtained by utilizing all motion data from all sensors. Additionally, the recognition performance using a minimal set of two sensors was also computed for comparison. This minimal set consisted of two hand-picked sensors that provided the Euler joint angles of the right forearm (RFA) and hips (H). The sensor positioned on the right forearm was chosen since the majority of individuals in all datasets were right-handed, and the sensor placed on the hips because all spinal movement originates from the hips. The purpose of these comparisons is to assess the method's capability to select the set of sensors that achieves superior recognition performance over configurations that include all 52 inertial sensors or a manually picked set of sensors.

The HMM ergodic and left-to-right topologies, along with a different number of hidden states, were evaluated to determine the best HMM settings for the gesture vocabulary defined in each dataset. Left-to-right HMM topology produced the best

TABLE X
SELECTED SENSORS FOR EACH DATASET.

Motion representation	Dataset						
	TVA	TVP	APA	GLB	MSC	SLW	ERGD
KF-GOM	LA, SP1, RUL	RSH1, LFA, SP2	RA, LSH1, LSH2, SP3, SP2, LUL, RUL	LSH2, RFA, H, SP3	LSH1, SP3, LUL, LL	RSH1, LSH1, HE, LUL, RL	LA, RSH1, LFA, SP2, RUL
KF-RGOM	LA, RFA, SP	LSH1, RFA, SP2	RA, LSH1, SP3, LUL	RSH1, RFA, SP1, RUL	LSH1, SP3, LL, LUL	LA, RA, SP, LUL, RL	RA, LSH1, RFA, SP1, LL
VAE-RGOM	LA, SP, LL	LA, RFA, SP	LA, SP2, LL	LA, LSH2, SP3, LL	LA, LSH2, SP3, LL	LA, LSH1, RFA, SP3, LL	LA, LSH1, RFA, SP3, LL
ATT-RGOM	LA, LSH1, H	LA, RFA, SP1	LA, LSH1, H	LSH1, LSH2, RFA, LUL	LSH2, RFA, LUL, LL	RA, LSH1, RFA, SP1, LL	RA, LSH1, RFA, SP1, LL

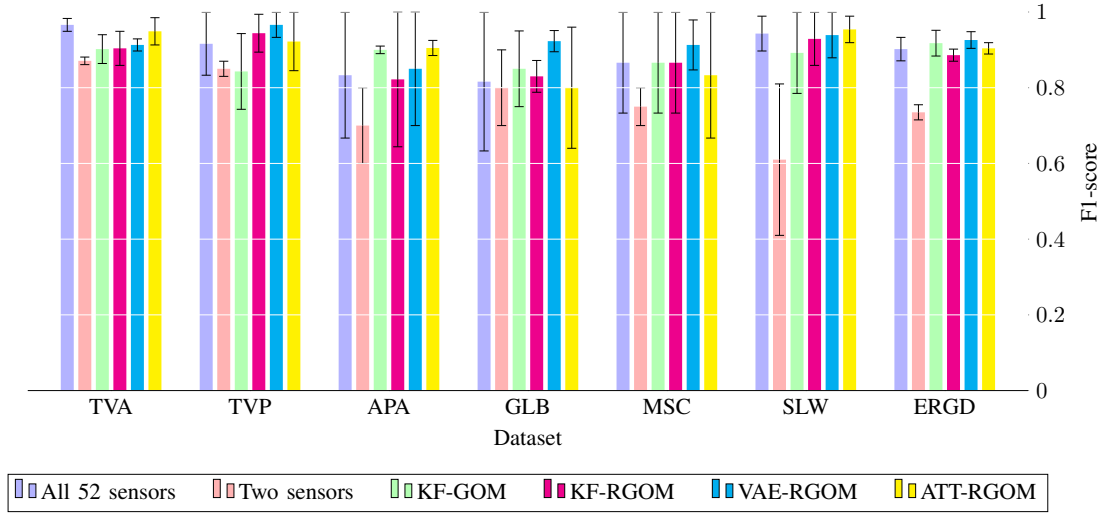


Fig. 10. F1-score of the recognition according to each selected set of sensors.

results for all recognition problems. Concerning the number of hidden states, it was defined for the HMMs of TVA and ERGD with seven states, TVP with six states, APA, GLB, and MSC with eight states, and SLW with three states. Table X illustrates the sensors selected for each dataset based on the motion representations generated by each approach. Then, Fig. 10 displays the calculated F1-scores for each sensor set per dataset.

The relevance of the sensors selected based on each approach for each dataset was demonstrated by the superior or similar recognition performance attained compared to using all sensor data. By observing Fig. 10, the best minimal set for TVA and SLW was determined by using the representations estimated by ATT-RGOM. These sensors achieved comparable results to using all sensors' data, having the ATT-RGOM set an F1-score of 0.949 for TVA, whereas all sensors set had an F1-score of 0.966. Then, for SLW, the ATT-RGOM sensor set performed at least 1% better than all other sensor sets.

VAE-RGOM representations provided the best sensor set for TVP, with an F1-score of 0.966. When comparing the sensors from the VAE-RGOM and ATT-RGOM sets, it is observed that the VAE-RGOM set included a sensor from the lower spine (SP). This sensor enhanced the ability to distinguish between

the motions of placing a box on the first and second levels.

The recognition of motions from APA was better using the data provided by the sensor sets of KF-RGOM and ATT-RGOM, although the ATT-RGOM sensor set contained fewer sensors. The set selected using ATT-RGOM representations attained an F1-score of 0.905, outperforming the set containing all sensor data. The APA motions were the most challenging to recognize. This may be because the motions in this vocabulary are more complex and prolonged. In addition, there is a substantial intra-class variance due to the fact that just one airplane structure was constructed for this dataset. There were no repetitions in which the pneumatic hammer was positioned in the same location more than once.

The glassblowing motions performed in GLB were better recognized using the data from the sensor sets estimated using VAE-RGOM representations, reaching an F1-score of 0.923. According to all GOM representations, the shoulders contribute the most to the execution of glassblowing motions, which is why the two-sensors configuration performed the worst. In addition, using the motion data measured from the left calf, which VAE-RGOM included, the recognition performance improved by at least 5% in the F1-score compared to all other sets.

The sensors picked using VAE-RGOM representations were also the most effective at discriminating motions from MSC and ERGD. These were the gesture vocabularies with the greatest number of classes. Because of this, the selected sensors for each recognition problem are similar. The VAE-RGOM sensor set attained an F1-score of 0.913 for MSC. Then, for ERGD, the VAE-RGOM sensor set achieved an F1-score of 0.926. The poor performance of the two-sensor configuration for MSC and ERGD may have been caused by its inability to differentiate between motions that differ only in the posture of the legs, as the motion data from the hips was insufficient.

VIII. CONCLUSION

In determining the optimal approach for modeling human movements, there is a trade-off to be considered between the accuracy of the modeling and the computing cost of the training procedure. VAE-RGOM and ATT-RGOM are able to simulate human motions more accurately and can be scaled to provide a greater variety of human motions. In addition, these approaches generate the representations of all full-body motion descriptors simultaneously, unlike KF-RGOM, which require modeling one motion descriptor at a time, meaning training separately 57 models (one per descriptor) for simulating full-body movements. Nevertheless, the training of VAE-RGOM and ATT-RGOM is data-intensive, necessitating a large volume of data depending on the architecture of the neural network and a significant amount of computing power. KF-RGOM, on the other hand, is sufficiently accurate to generate specific human motions using one-shot training. This training strategy enables users to specify the human motion and motion descriptors to be analyzed. Then construct their mathematical representation according to GOM using straightforward procedures that demand less computational power than data-driven methods.

The results demonstrated the ability of the proposed approaches to explain how a motion is conducted in accordance with GOM's assumptions, and identified the most significant motion descriptors. As potential future work, the proposed analytical models can be integrated with neurophysiological techniques that, for example, account for muscle activity and motor cortex activity. This combination would allow for a more thorough approach that could provide a neurophysiological roadmap of complex body dexterity. However, because of the inherent complexity and the sheer amount of data it requires, such a complete study that considers all these neurophysiological factors hasn't been done to this point. Lastly, it is neither feasible nor practicable to employ a full-body MoCap suit in many human motion analysis applications. Determining the minimal motion descriptors to measure allows for the adoption of less invasive technologies, such as smartphones and smartwatches, that could also measure these motion descriptors.

ACKNOWLEDGMENTS

The research leading to these results has received funding by the EU Horizon 2020 Research and Innovation Programme

under Grant Agreement No. 820767, CoLLaboratE project, and Grant No. 822336, Mingei project.

REFERENCES

- [1] A. Muller, C. Pontonnier, X. Robert-Lachaine, G. Dumont, and A. Plamondon, "Motion-based prediction of external forces and moments and back loading during manual material handling tasks," *Applied Ergonomics*, vol. 82, no. August 2019, p. 102935, 2020. [Online]. Available: <https://doi.org/10.1016/j.apergo.2019.102935>
- [2] G. S. Faber, C. C. Chang, I. Kingma, J. T. Dennerlein, and J. H. van Dieën, "Estimating 3D L5/S1 moments and ground reaction forces during trunk bending using a full-body ambulatory inertial motion capture system," *Journal of Biomechanics*, vol. 49, no. 6, pp. 904–912, 2016. [Online]. Available: <http://dx.doi.org/10.1016/j.jbiomech.2015.11.042>
- [3] D. Menychtas, A. Glushkova, and S. Manitsaris, "Analyzing the kinematic and kinetic contributions of the human upper body's joints for ergonomics assessment," *Journal of Ambient Intelligence and Humanized Computing*, pp. 1–23, 2020.
- [4] F. G. Larsen, F. P. Svenningsen, M. S. Andersen, M. de Zee, and S. Skals, "Estimation of Spinal Loading During Manual Materials Handling Using Inertial Motion Capture," *Annals of Biomedical Engineering*, vol. 48, no. 2, pp. 805–821, 2020. [Online]. Available: <http://link.springer.com/10.1007/s10439-019-02409-8>
- [5] A. Barth and U. Franke, "Where will the oncoming vehicle be the next second?" in *2008 IEEE Intelligent Vehicles Symposium*, 2008, pp. 1068–1073.
- [6] E. Binelli, A. Broggi, A. Fascioli, S. Ghidoni, P. Grisleri, T. Graf, and M. Meinecke, "A modular tracking system for far infrared pedestrian recognition," in *IEEE Proceedings. Intelligent Vehicles Symposium*, 2005., 2005, pp. 759–764.
- [7] B. Caramiaux, N. Montecchio, A. Tanaka, and F. Bevilacqua, "Adaptive Gesture Recognition with Variation Estimation for Interactive Systems," *ACM Transactions on Interactive Intelligent Systems*, vol. 4, no. 4, pp. 1–34, 2015. [Online]. Available: <https://dl.acm.org/doi/10.1145/2643204>
- [8] A. Glushkova and S. Manitsaris, "Gesture recognition and sensorimotor learning-by-doing of motor skills in manual professions: A case study in the wheel-throwing art of pottery," *Journal of Computer Assisted Learning*, vol. 34, no. 1, pp. 20–31, 2018.
- [9] A. Malaisé, P. Maurice, F. Colas, F. Charpillet, A. Malaisé, P. Maurice, F. Colas, F. Charpillet, S. I. A. Recog, A. Malais, P. Maurice, F. Colas, and S. Ivaldi, "Activity Recognition With Multiple Wearable Sensors for Industrial Applications," in *ACHI 2018 - Eleventh International Conference on Advances in Computer-Human Interactions*, 2018, pp. 1–7.
- [10] S. Manitsaris, G. Senter, D. Makrygiannis, and A. Glushkova, "Human movement representation on multivariate time series for recognition of professional gestures and forecasting their trajectories," *Frontiers in Robotics and AI*, vol. 7, pp. 1–20, 2020.
- [11] Z. Wang, K. Mülling, M. P. Deisenroth, H. Ben Amor, D. Vogt, B. Schölkopf, and J. Peters, "Probabilistic movement modeling for intention inference in human-robot interaction," *International Journal of Robotics Research*, vol. 32, no. 7, pp. 841–858, 2013.
- [12] M. Devanne, S. Berretti, P. Pala, H. Wannous, M. Daoudi, and A. Del Bimbo, "Motion segment decomposition of RGB-D sequences for human behavior understanding," *Pattern Recognition*, vol. 61, pp. 222–233, 2017. [Online]. Available: <http://dx.doi.org/10.1016/j.patcog.2016.07.041>
- [13] P. L. Davidson, D. J. Chalmers†, and B. D. Wilson‡, "Stochastic-rheological Simulation of Free-fall Arm Impact in Children: Application to Playground Injuries," *Computer Methods in Biomechanics and Biomedical Engineering*, vol. 7, no. 2, pp. 63–71, apr 2004. [Online]. Available: <http://www.tandfonline.com/doi/abs/10.1080/1025584042000206461>
- [14] J. E. Langenderfer, J. E. Carpenter, M. E. Johnson, K.-n. An, and R. E. Hughes, "A Probabilistic Model of Glenohumeral External Rotation Strength for Healthy Normals and Rotator Cuff Tear Cases," *Annals of Biomedical Engineering*, vol. 34, no. 3, pp. 465–476, mar 2006. [Online]. Available: <http://link.springer.com/10.1007/s10439-005-9045-9>
- [15] C.-F. Lin, H. Liu, M. T. Gros, P. Weinhold, W. E. Garrett, and B. Yu, "Biomechanical risk factors of non-contact ACL injuries: A stochastic biomechanical modeling study," *Journal of Sport and Health Science*, vol. 1, no. 1, pp. 36–42, 2012. [Online]. Available: <https://linkinghub.elsevier.com/retrieve/pii/S2095254612000129>

- [16] D. M. S. Donnell, J. L. Seidelman, C. L. Mendias, B. S. Miller, J. E. Carpenter, and R. E. Hughes, "A stochastic structural reliability model explains rotator cuff repair retears," *International Biomechanics*, vol. 1, no. 1, pp. 29–35, 2014. [Online]. Available: <http://dx.doi.org/10.1080/23310472.2014.983166>
- [17] X. Shu, L. Zhang, G.-J. Qi, W. Liu, and J. Tang, "Spatiotemporal Co-Attention Recurrent Neural Networks for Human-Skeleton Motion Prediction," *IEEE Transactions on Pattern Analysis and Machine Intelligence*, vol. 44, no. 6, pp. 3300–3315, 2022. [Online]. Available: <https://ieeexplore.ieee.org/document/9321130/>
- [18] W. Mao, M. Liu, M. Salzmann, and H. Li, "Multi-level Motion Attention for Human Motion Prediction," *International Journal of Computer Vision*, vol. 129, no. 9, pp. 2513–2535, sep 2021. [Online]. Available: <https://link.springer.com/10.1007/s11263-021-01483-7>
- [19] Y. Cai, L. Huang, Y. Wang, T.-J. Cham, J. Cai, J. Yuan, J. Liu, X. Yang, Y. Zhu, X. Shen, D. Liu, J. Liu, and N. M. Thalmann, "Learning progressive joint propagation for human motion prediction," in *Computer Vision – ECCV 2020*, A. Vedaldi, H. Bischof, T. Brox, and J.-M. Frahm, Eds. Cham: Springer International Publishing, 2020, pp. 226–242.
- [20] S. Aliakbarian, F. Saleh, L. Petersson, S. Gould, and M. Salzmann, "Contextually Plausible and Diverse 3D Human Motion Prediction," in *2021 IEEE/CVF International Conference on Computer Vision (ICCV)*. IEEE, 2021, pp. 11 313–11 322. [Online]. Available: <http://arxiv.org/abs/1912.08521https://ieeexplore.ieee.org/document/9710194/>
- [21] W. Mao, M. Liu, and M. Salzmann, "Generating Smooth Pose Sequences for Diverse Human Motion Prediction," in *2021 IEEE/CVF International Conference on Computer Vision (ICCV)*. IEEE, oct 2021, pp. 13 289–13 298. [Online]. Available: <https://ieeexplore.ieee.org/document/9711405/>
- [22] J. Chung, K. Kastner, L. Dinh, K. Goel, A. Courville, and Y. Bengio, "A recurrent latent variable model for sequential data," in *Proceedings of the 28th International Conference on Neural Information Processing Systems - Volume 2*, ser. NIPS'15. Cambridge, MA, USA: MIT Press, 2015, p. 2980–2988.
- [23] M. Fraccaro, S. K. Sønderby, U. Paquet, and O. Winther, "Sequential Neural Models with Stochastic Layers," *Advances in Neural Information Processing Systems*, pp. 2207–2215, 2016. [Online]. Available: <http://arxiv.org/abs/1605.07571>
- [24] D. Salinas, V. Flunkert, and J. Gasthaus, "DeepAR: Probabilistic Forecasting with Autoregressive Recurrent Networks," 2017. [Online]. Available: <http://arxiv.org/abs/1704.04110>
- [25] X. Liu, J. Yin, H. Liu, and J. Liu, "DeepSSM: Deep State-Space Model for 3D Human Motion Prediction," *arXiv e-prints*, 2020. [Online]. Available: <http://arxiv.org/abs/2005.12155>
- [26] B. E. Olivas-Padilla, S. Manitsaris, D. Menychtas, and A. Glushkova, "Stochastic-biomechanic modeling and recognition of human movement primitives, in industry, using wearables," *Sensors*, vol. 21, no. 7, 2021.
- [27] C. Ionescu, D. Papava, V. Olaru, and C. Sminchisescu, "Human3.6m: Large scale datasets and predictive methods for 3d human sensing in natural environments," *IEEE Transactions on Pattern Analysis and Machine Intelligence*, vol. 36, no. 7, pp. 1325–1339, 2014.
- [28] Carnegie Mellon University, "CMU Graphics Lab Motion Capture Database." [Online]. Available: <http://mocap.cs.cmu.edu/>
- [29] N. Mahmood, N. Ghorbani, N. F. Troje, G. Pons-Moll, and M. J. Black, "AMASS: Archive of motion capture as surface shapes," in *International Conference on Computer Vision*, 2019, pp. 5442–5451.
- [30] L. Sigal, A. O. Balan, and M. J. Black, "HumanEva: Synchronized video and motion capture dataset and baseline algorithm for evaluation of articulated human motion," *International Journal of Computer Vision*, vol. 87, no. 1-2, pp. 4–27, 2010.
- [31] S. Ghorbani, K. Mahdavian, A. Thaler, K. Kording, D. J. Cook, G. Blohm, and N. F. Troje, "MoVi: A large multi-purpose human motion and video dataset," *PLoS ONE*, vol. 16, no. 6 June, 2021. [Online]. Available: <http://dx.doi.org/10.1371/journal.pone.0253157>
- [32] J. Snoek, H. Larochelle, and R. P. Adams, "Practical bayesian optimization of machine learning algorithms," in *Advances in Neural Information Processing Systems*, F. Pereira, C. Burges, L. Bottou, and K. Weinberger, Eds., vol. 25. Curran Associates, Inc., 2012. [Online]. Available: <https://proceedings.neurips.cc/paper/2012/file/05311655a15b75fab86956663e1819cd-Paper.pdf>